

# S2WMamba: A Spectral-Spatial Wavelet Mamba for Pansharpening

Haoyu Zhang<sup>1\*</sup> Junhan Luo<sup>1\*</sup> Yugang Cao<sup>1\*</sup> Jie Huang<sup>1</sup> Liangjian-Deng<sup>1†</sup>

<sup>1</sup>University of Electronic Science and Technology of China

{2024090908014, 2024310207017, 2024080301024, jayhuang}@std.uestc.edu.cn,  
liangjian.deng@uestc.edu.cn

## Abstract

Pansharpening fuses a high-resolution PAN image with a low-resolution multispectral (LRMS) image to produce an HRMS image. A key difficulty is that jointly processing PAN and MS often entangles spatial detail with spectral fidelity. We propose S2WMamba, which explicitly disentangles frequency information and then performs lightweight cross-modal interaction. Concretely, a 2D Haar DWT is applied to PAN to localize spatial edges and textures, while a channel-wise 1D Haar DWT treats each pixel’s spectrum as a 1D signal to separate low/high-frequency components and limit spectral distortion. The resulting Spectral branch injects wavelet-extracted spatial details into MS features, and the Spatial branch refines PAN features using spectra from the 1D pyramid; the two branches exchange information through Mamba-based cross-modulation that models long-range dependencies with linear complexity. A multi-scale dynamic gate (multiplicative + additive) then adaptively fuses branch outputs. On WV3, GF2, and QB, S2WMamba matches or surpasses recent strong baselines (FusionMamba, CANNet, U2Net, ARConv), improving PSNR by up to 0.23 dB and reaching HQNR 0.956 on full-resolution WV3. Ablations justify the choice of 2D/1D DWT placement, parallel dual branches, and the fusion gate. Our code is available at <https://github.com/KagUYa66/S2WMamba>.

## 1. Introduction

High-resolution multispectral (HRMS) images are vital for applications in environmental monitoring and urban planning. Owing to hardware constraints, satellites typically capture two types of images: low-resolution multispectral (LRMS) images with rich spectral information and high-resolution panchromatic (PAN) images with fine spatial details. Pansharpening aims to fuse these two sources to gen-

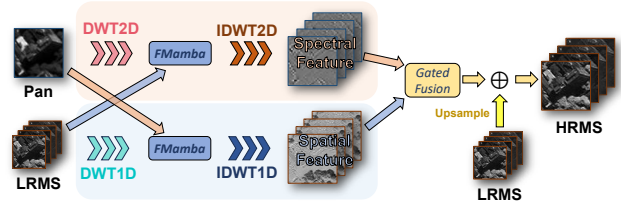


Figure 1. This figure illustrates our dual-branch framework. The spectral branch processes PAN images using a 2D DWT, while the spatial branch handles LRMS images with a 1D DWT. Both branches leverage SSM (Mamba) for fusion before reconstruction.

erate an HRMS image that combines the strengths of both, achieving high resolution in both the spatial and spectral domains.

Pansharpening methods are broadly categorized into traditional and deep-learning-based approaches. Traditional methods include Component Substitution (CS) [26], Multi-Resolution Analysis (MRA) [27], and Variational Optimization-based (VO) techniques [24]. Although foundational, these methods often struggle with the trade-off between spatial detail injection and spectral consistency, leading to artifacts. In recent years, deep learning has driven significant progress. Convolution-based models (e.g., PNN [19] and MSDCNN [15]) excel at extracting local features but are constrained by limited receptive fields, hindering the modeling of the global context. Transformer-based approaches (e.g., PanFormer [33]) capture long-range dependencies but suffer from quadratic complexity [25] and can introduce block artifacts.

Beyond standard CNNs and Transformers, several recent lines of work pursue stronger priors and more efficient global modeling. In the broader vision community, visual state space models such as VMamba [16] and Mamba-Adaptor [31] demonstrate that Mamba-style selective SSMS can serve as competitive backbones for classification, segmentation, and detection while maintaining global receptive fields and linear-time complexity. Architectures such as PanMamba [10] and FusionMamba [23] in-

\*Equal contribution.

†Corresponding author.

roduce State Space Models (Mamba) [9] into pansharpening and remote sensing image fusion, achieving favorable accuracy–efficiency trade-offs but still operating on spatially and spectrally entangled features, so enhancing one domain can compromise the other. Content-adaptive non-local convolutions [6] approximate non-local attention with dynamic kernels, enabling efficient long-range aggregation but still working in a fully shared spatial–spectral feature space. Architectures that couple Invertible Neural Networks (INNs) with customized Transformers [34] achieve information-preserving mappings and strong reconstruction guarantees while reducing parameter counts, and ARConv-style large-receptive-field convolutions further enhance efficiency compared to vanilla self-attention. However, despite their strengths, these approaches still process spatial and spectral information in a shared feature space, which makes it difficult to reason about and explicitly control the trade-off between spatial enhancement and spectral fidelity.

A parallel line of work has utilized wavelet transforms [18], which inherently decompose images into multi-scale frequency sub-bands, making them ideal for detail preservation and interpretable analysis. Building on this idea, recent pansharpening networks explicitly operate in the wavelet domain, for example wavelet-assisted multi-frequency attention networks that couple discrete wavelet transforms with frequency-aware attention mechanisms [13], cross-band transformers on wavelets that model inter-band dependencies in the transformed domain [20], and wavelet convolutional neural networks that embed DWT into convolutional filters [7]. However, many wavelet-based methods still rely on relatively shallow fusion strategies between PAN and LRMS wavelet coefficients, failing to fully capture the complex, non-linear interactions between frequency components from the PAN and LRMS images. This leads to two critical, unaddressed challenges: (1) **Feature Entanglement**: jointly processing PAN and LRMS features creates a tug-of-war between spatial enhancement and spectral fidelity, where improving one often degrades the other. (2) **Inadequate Frequency Fusion**: simple fusion mechanisms cannot adaptively weight and integrate frequency-specific information, resulting in suboptimal detail enhancement and color preservation even when the wavelet decomposition itself is well motivated.

To address the spatial–spectral trade-off in pansharpening, we introduce **S2WMamba**, a framework that explicitly bridges the spatial and spectral domains through principled feature disentanglement in the wavelet domain combined with efficient State Space Models (SSMs). Built on custom 1D/2D DWT–IDWT modules, our end-to-end architecture decomposes images into frequency subbands for targeted processing. A dual-branch design performs spectral fusion by injecting PAN-derived spatial details into LRMS subbands and spatial refinement via channel-

wise 1D DWT guided by PAN. A Multi-Scale Dynamic Gate adaptively merges these enhanced features, yielding high-resolution multispectral images with both spatial sharpness and spectral fidelity. By combining wavelet-domain feature disentanglement with SSM-based long-range modeling, S2WMamba offers a complementary perspective to content-adaptive non-local convolutions [30], INN-enhanced Transformers, and ARConv-style convolutions.

In summary, our main contributions are:

- A novel pansharpening framework, **S2WMamba**, that integrates wavelet transforms with State Space Models to explicitly disentangle and fuse features in the frequency domain. Its dual-branch design systematically addresses the trade-off between spatial detail and spectral consistency.
- A bespoke FMamba module (adapted from [23]) that models long-range, cross-modal interactions within decoupled wavelet subbands, enabling precise feature alignment between PAN and LRMS data with linear computational complexity.
- A Multi-Scale Dynamic Gate for adaptive feature fusion, which robustly merges the spatial and spectral streams by extracting features at multiple scales to mitigate information loss during reconstruction.
- State-of-the-art performance on multiple benchmark pansharpening datasets, with experiments demonstrating superior results in both quantitative metrics and qualitative visual comparisons.

## 2. Proposed Method

To address the spatial-spectral trade-off, we introduce S2WMamba, a framework for feature disentanglement in the wavelet domain. As shown in Fig. 2, its architecture comprises a dual-branch structure—a 2D DWT-guided **Spectral Branch** and a 1D DWT-guided **Spatial Branch**—whose outputs are merged by a **Multi-Scale Dynamic Gate (MSDG)**. The core modality fusion within this framework is powered by our bespoke FMamba modules.

### 2.1. FMamba: Fusing Modalities with Mamba

State-Space Models (SSMs) enable linear-time sequence processing. Given two same-shape feature maps  $X, Y \in \mathbb{R}^{C \times h \times w}$ , we form raster-scan sequences  $x, y \in \mathbb{R}^{N \times d}$  with  $N = hw$  (row-major). Each FMamba block contains *two* modules: (i) a *self* Mamba on each stream and (ii) a *cross* Mamba where the other stream enters as an auxiliary *modulator*. Concretely, with pre-LayerNorm and linear projec-

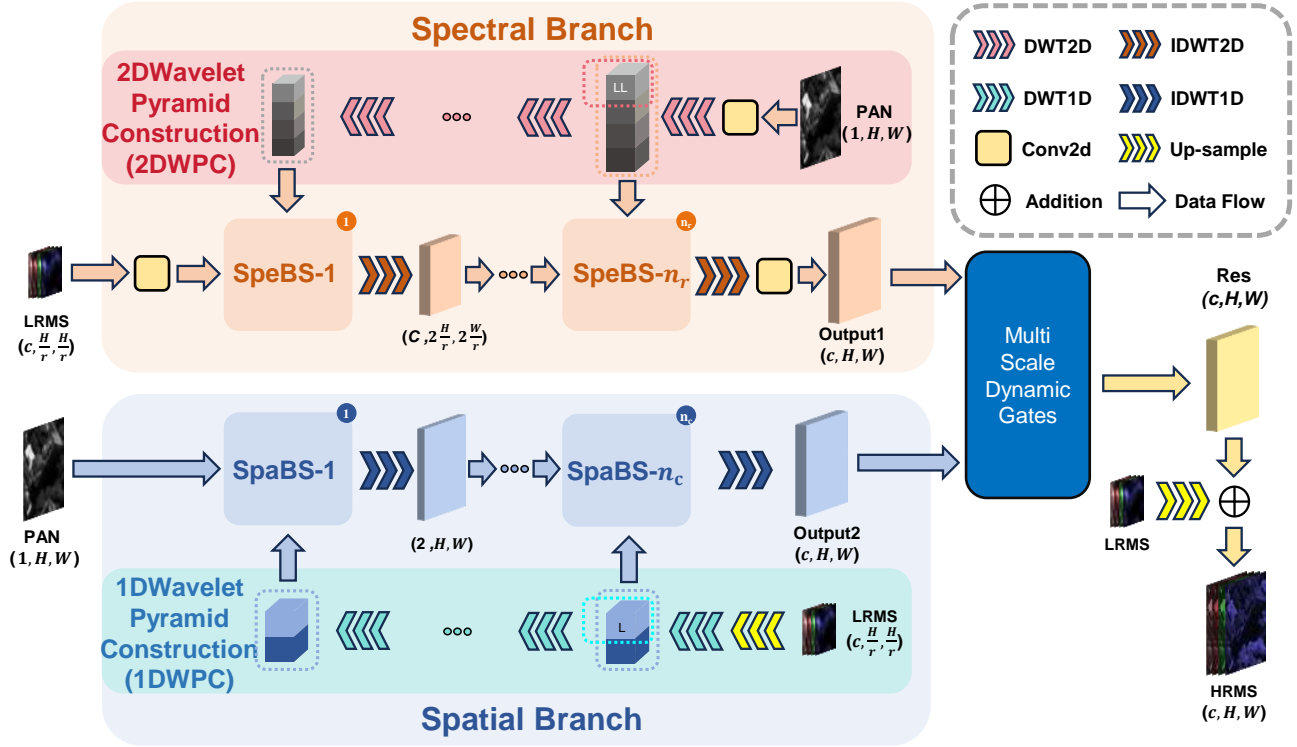


Figure 2. The overall workflow of our S2WMamba. Our network consists of three main components: a Spectral Branch, a Spatial Branch, and a Multi-Scale Dynamic Gate (MSDG) Block. The 2D Wavelet Pyramid Construction (2DWPC) and the 1D Wavelet Pyramid Construction (1DWPC) respectively provide spatial or spectral details for further fusion in Spectral or Spatial Branch.

tions  $\phi(\cdot)$ ,

$$\tilde{x} = \phi(\text{LN}(x)) + x, \quad \tilde{y} = \phi(\text{LN}(y)) + y, \quad (1)$$

$$\hat{x} = \text{Cross-Mamba}(\tilde{x} | \tilde{y}), \quad \hat{y} = \text{Cross-Mamba}(\tilde{y} | \tilde{x}), \quad (2)$$

$$f = \hat{x} + \hat{y} + \sigma(\alpha) x + (1 - \sigma(\alpha)) y, \quad (3)$$

where the cross module takes the auxiliary embedding as an extra input to modulate state updates;  $\sigma$  is the logistic sigmoid and  $\alpha$  is a learned scalar balancing residual skip from two streams. We do not inject explicit positional encodings; 2D sizes  $(h, w)$  are passed to the Mamba kernel (our implementation) so that gated convolutions inside SSM respect the spatial layout. All Mamba blocks are linear in  $N$  both in time and memory, which is critical for high-resolution inputs.

## 2.2. Channel-wise 1D Discrete Wavelet Transform (DWT1D)

A primary source of spectral distortion in pansharpening is the naive fusion of spectrally rich and spatially detailed features. To counteract this, we introduce a 1D Discrete Wavelet Transform applied along the channel dimension

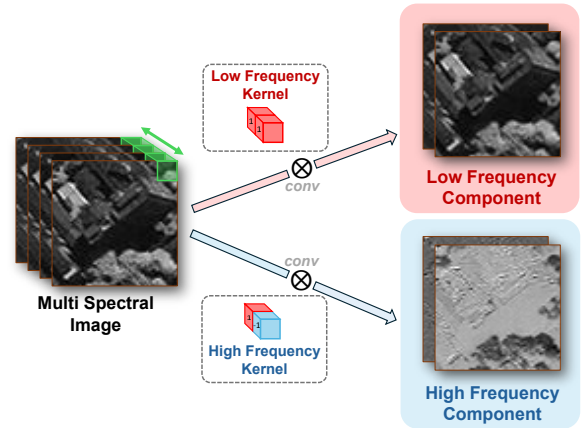


Figure 3. An illustration of the core wavelet decomposition strategies. The 2D DWT (top) is applied to the spatial dimensions of an image, decomposing it into four frequency sub-bands. The 1D DWT (bottom) is applied along the channel axis, disentangling the spectral information into low- and high-frequency components.

(DWT1D), as illustrated in Fig. 3. The core motivation is to treat the spectral signature of each pixel—a vector of

Table 1. Spectral Branch: stage-wise tensors (all batches omitted for brevity),  $r=4$  (for WV3, GF2 and QB)

Input PAN conv	$P \in \mathbb{R}^{C \times H \times W}$
Level-1 DWT2D	$[LL_1, LH_1, HL_1, HH_1] \in \mathbb{R}^{4C \times \frac{H}{2} \times \frac{W}{2}}$
Level-2 DWT2D	$[LL_2, LH_2, HL_2, HH_2] \in \mathbb{R}^{4C \times \frac{H}{4} \times \frac{W}{4}}$
FMamba (SpeBS-1)	$[F_{LL_1}, F_{LH_1}, F_{HL_1}, F_{HH_1}] \in \mathbb{R}^{4C \times \frac{H}{4} \times \frac{W}{4}}$
IDWT2D (SpeBS-1)	$M_1 \in \mathbb{R}^{C \times \frac{H}{2} \times \frac{W}{2}}$
FMamba (SpeBS-2)	$[F_{LL_2}, F_{LH_2}, F_{HL_2}, F_{HH_2}] \in \mathbb{R}^{4C \times \frac{H}{2} \times \frac{W}{2}}$
IDWT2D (SpeBS-2)	$M_2 \in \mathbb{R}^{C \times H \times W}$
Reduce to $c$	$S \in \mathbb{R}^{c \times H \times W}$

channel intensities—as a 1D signal. This perspective allows us to decompose the signal into its foundational low-frequency components, representing coarse spectral characteristics, and its high-frequency components, capturing the finer inter-band variations and details.

Our implementation is a fully differentiable module. For an input feature map  $\mathbf{X} \in \mathbb{R}^{B \times C \times H \times W}$ , we apply predefined Haar wavelet filters via 1D convolution along the channel axis. This operation, denoted as  $\{\mathbf{L}, \mathbf{H}\} = \text{DWT1D}(\mathbf{X})$ , splits  $\mathbf{X}$  into a low-frequency sub-band  $\mathbf{L} \in \mathbb{R}^{B \times (C/2) \times H \times W}$  and a high-frequency sub-band  $\mathbf{H} \in \mathbb{R}^{B \times (C/2) \times H \times W}$ . The transformation is perfectly reversible via an Inverse 1D DWT (IDWT1D). This channel-wise decomposition is the cornerstone of our Spatial Branch, enabling a controlled, multi-scale injection of spectral information that enhances spatial structures while rigorously preserving spectral integrity.

### 2.3. Spectral Branch: Hierarchical Spatial Detail Injection

The Spectral Branch is engineered to enrich the LRMS image with fine-grained spatial details extracted from the PAN image. This is accomplished through a hierarchical framework that operates entirely in the 2D wavelet domain.

#### 2.3.1. 2D Wavelet Pyramid Construction (2DWPC)

To create a multi-scale repository of spatial information, the PAN image is first passed through a convolutional layer. The resulting feature map is then hierarchically decomposed for  $n_r = \log_2(r)$  levels using a 2D DWT, where  $r$  is the spatial resolution ratio. At each decomposition level  $i$ , the low-frequency component from the previous level,  $LL_{i-1}$ , is split into four sub-bands: a low-frequency approximation ( $LL_i$ ) and three high-frequency detail components ( $LH_i, HL_i, HH_i$ ), described as:

$$\{LL_i, LH_i, HL_i, HH_i\} = \text{DWT2D}(LL_{i-1}), \quad i = 1, \dots, n_r, \\ \text{with } LL_0 = \text{Conv}(\text{PAN}) \quad (4)$$

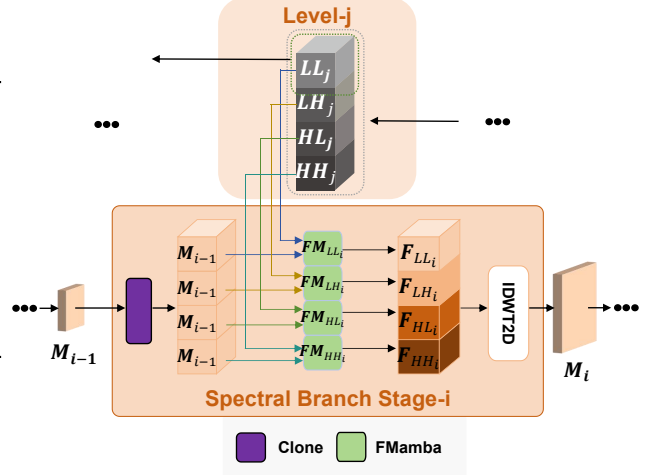


Figure 4. The workflow of a representative Spectral Branch Stage (e.g., Stage- $i$ ) is depicted here. This structure is identically applied to all  $n_r$  stages, in addition to the size of the input. The input to SpeBS- $i$  consists of the output of the previous stage, along with one set of sub-bands from the 2DWPC. The decomposition level of the sub-bands in 2DWPC is  $n_r - i + 1$  so that each sub-band shares the same resolution with  $M_{i-1}$ . Here,  $j$  is used to represent the corresponding 2D DWT decomposition level in 2DWPC, with the relation  $j = n_r - i + 1$ . FM here represent FMamba Block.

#### 2.3.2. Spectral Branch Stages (SpeBS) for Hierarchical Fusion

The fusion and reconstruction occur progressively across  $n_r$  Spectral Branch Stages (SpeBS), each denoted as SpeBS-1,  $\dots$ , SpeBS- $n_r$  for clarity. Let  $M_0$  represent the convolved LRMS input. The output of the  $k$ th stage is denoted as  $M_k$ . As shown in Fig. 4, each stage  $i$  is designed to fuse the output from former stage  $M_{i-1}$  with a set of spatial frequency sub-bands from the 2DWPC at decomposition level  $n_r - i + 1$  so that their resolution matches. The fusion is conducted using four parallel FMamba, each dedicated to integrating a specific spatial frequency component with the spectral features:

$$F_{s_i} = \text{FMamba}_{s_i}(M_{i-1}, s_j), \quad s \in \{LL, LH, HL, HH\} \quad (5)$$

where  $j = n_r - i + 1$ . The four enriched sub-bands are then synthesized via a 2D IDWT, reconstructing the feature map  $M_i$  at double the spatial resolution of  $M_{i-1}$ . This iterative refinement continues for  $n_r$  stages, culminating in a feature map  $M_{n_r}$  at the full PAN resolution, with a final convolution layer adjusting the channel of  $M_{n_r}$  to original LRMS channel dimension, producing **Output1**—a spectrally-grounded map enhanced with multi-scale spatial details.

## 2.4. Spatial Branch: Guided Spectral Refinement

Complementing the Spectral Branch, this branch refines the PAN image’s spatial structure by injecting learned spectral information derived from both the original LRMS image and the spatially-enhanced **Output1**. It mirrors the hierarchical strategy of the Spectral Branch but operates in the channel-spectral domain using our novel 1D DWT.

### 2.4.1. 1D Wavelet Pyramid Construction (1DWPC)

The 1DWPC module decomposes the spectral information into a multi-level frequency pyramid. Its input,  $L_0 = \text{Upsample}(\text{LRMS}) + \text{Output1}$ , combines the original spectral data with the enhanced features from the Spectral Branch. This combined map is hierarchically decomposed for  $n_c = \log_2(c)$  levels via our 1D DWT, where  $c$  is the number of LRMS channels. At each decomposition level  $i$ , the low-frequency component from the previous level,  $L_{i-1}$ , is split into two sub-bands: low-frequency ( $L_i$ ) and high-frequency ( $H_i$ ), described as:

$$\{L_i, H_i\} = \text{DWT1D}(L_{i-1}), \quad i = 1, 2, \dots, n_c \quad (6)$$

### 2.4.2. Spatial Branch Stages (SpaBS) for Hierarchical Fusion

The spatial refinement is performed across  $n_c$  Spatial Branch Stages (SpaBS), denoted as SpaBS-1, ..., SpaBS- $n_c$  for clarity. Let  $P_0$  be the initial PAN image. As detailed in Fig. 5, at each stage  $i$ , the SpaBS- $i$  takes the previous stage’s output  $P_{i-1}$  and a set of spectral frequency components  $\{L_j, H_j\}$  from the 1DWPC pyramid, where  $j = n_c - i + 1$ . These inputs are projected to a common dimension and fused using two parallel FMamba blocks, allowing the PAN stream to be modulated by spectral characteristics:

$$\begin{aligned} F_{L_i} &= \text{FMamba}_{L_i}(\text{Conv}_C(P_{i-1}), \text{Conv}_C(L_j)) \\ F_{H_i} &= \text{FMamba}_{H_i}(\text{Conv}_C(P_{i-1}), \text{Conv}_C(H_j)) \end{aligned} \quad (7)$$

where  $\text{Conv}_C(\cdot)$  denotes a 2D convolution that maps inputs to the feature dimension  $C$ . The fused features are projected back to their original dimensions and reconstructed via a 1D IDWT:

$$P_i = \text{IDWT1D}(\text{Conv}_{\text{orig}}(F_{L_i}), \text{Conv}_{\text{orig}}(F_{H_i})) \quad (8)$$

This iterative process doubles the number of channels at each stage. The final output  $P_{n_c}$ , denoted as **Output2**, is a spatially-refined map with the same channel dimension as the LRMS image ready for final fusion.

## 2.5. Multi-Scale Dynamic Gate (MSDG) Block

Recognizing that a static or linear combination of the two specialized branch outputs would be suboptimal, we propose the Multi-Scale Dynamic Gate (MSDG). The MSDG

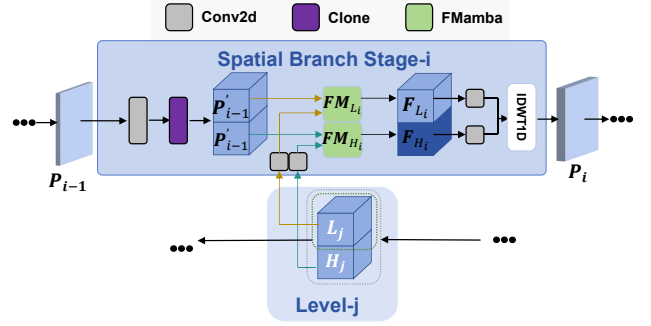


Figure 5. The workflow of a representative Spatial Branch Stage (e.g., Stage- $i$ ) is depicted here. This structure is identically applied to all  $n_c$  stages, in addition to the size of the input. The input to SpaBS- $i$  consists of the output of the previous stage ( $P_{i-1}$ ), along with one set of sub-bands from 1DWPC. The decomposition level of the sub-bands is  $n_c - i + 1$  so that each sub-band shares the same channel with  $P_{i-1}$ . Here,  $j$  is used to represent the corresponding decomposition level in 1DWPC, with the relation  $j = n_c - i + 1$ .

Table 2. Spatial Branch: channel-wise DWT1D on  $C$  bands (non-interleaved [L,H] layout).

$c=8$ (WV3): $n_c=3$	
Level-3 DWT1D: $L_1, H_1$	$\mathbb{R}^{1 \times H \times W}$
$\text{IDWT1D}(\text{SpaBS} - 1)$	$\mathbb{R}^{2 \times H \times W}$
Level-2 DWT1D: $L_2, H_2$	$\mathbb{R}^{2 \times H \times W}$
$\text{IDWT1D}(\text{SpaBS} - 2)$	$\mathbb{R}^{4 \times H \times W}$
Level-1 DWT1D: $L_3, H_3$	$\mathbb{R}^{4 \times H \times W}$
$\text{IDWT1D}(\text{SpaBS} - 3)$	$\mathbb{R}^{8 \times H \times W}$
$c=4$ (GF2/QB): $n_c=2$	
Level-2 DWT1D: $L_2, H_2$	$\mathbb{R}^{1 \times H \times W}$
$\text{IDWT1D}(\text{SpaBS} - 1)$	$\mathbb{R}^{2 \times H \times W}$
Level-1 DWT1D: $L_1, H_1$	$\mathbb{R}^{2 \times H \times W}$
$\text{IDWT1D}(\text{SpaBS} - 2)$	$\mathbb{R}^{4 \times H \times W}$

integrates three key mechanisms: an Interactive Enhancement Block (IEB) for bidirectional feature refinement, an  $n \times n$  Regional Feature Extracting Block (RFEB) to capture local textural patterns at multiple scales, and a Global Feature Extracting Block (GFEB) to encode global context. The MSDG first enhances its two inputs, **Output1** ( $\mathbf{X}_{\text{main}}$ ) and **Output2** ( $\mathbf{X}_{\text{extra}}$ ), using the IEB. The refined features are concatenated, normalized, and processed in parallel by RFEBs (with  $1 \times 1$  and  $3 \times 3$  kernels in our implementation) and the GFEB. The aggregated local and global features generate a unified gate tensor, which is then split into three distinct components: a multiplicative gate  $\mathbf{G}_{\text{mul}}$ , a decorative gate  $\mathbf{G}_{\text{dec}}$ , and an additive gate  $\mathbf{G}_{\text{add}}$ . These gates orchestrate a complex, nonlinear fusion:

$$\text{MSDGout} = \mathbf{X}_{\text{main}} \odot (1 + \mathbf{G}_{\text{dec}} + \mathbf{G}_{\text{mul}} \odot \mathbf{X}_{\text{extra}}) + \mathbf{G}_{\text{add}} \quad (9)$$

where  $\odot$  denotes the Hadamard product. This formulation allows for a highly adaptive, spatially varying fusion where features from one branch can dynamically amplify, attenuate, or embellish features from the other on a per-pixel basis, transcending the limitations of simple additive or concatenative approaches. We use two gates in the S2WMamba, and we also use an adaptive rate to softly swap the roles of the two gates.

## 2.6. Network Framework and Loss Function

The overall S2WMamba framework synthesizes the final pansharpened image in a residual learning paradigm [11]. The MSDG block fuses the intermediate results **Output**<sub>1</sub> and **Output**<sub>2</sub> to produce a residual image **Res**. This residual is then added to the upsampled LRMS image to yield the final result:  $\mathbf{HRMS} = \mathbf{LRMS}_{\text{upsampled}} + \mathbf{Res}$ . The entire network is trained end-to-end by minimizing the Mean Absolute Error ( $\ell_1$  loss) between the predicted HRMS and the ground truth (GT), a loss function proven effective for promoting sharpness in image restoration tasks [3, 14]:

$$\mathcal{L} = \frac{1}{K} \sum_{i=1}^K \left\| \hat{M}^{\{i\}} - I^{\{i\}} \right\|_1 \quad (10)$$

where  $K$  is the number of training samples,  $\hat{M}^{\{i\}}$  is the network’s output, and  $I^{\{i\}}$  is the corresponding ground truth image.

## 3. Experiments

### 3.1. Comparison to the State of the Art

Compared with recent pansharpening systems, S2WMamba differs in three aspects. (1) Versus Transformer-based PanFormer, our FMamba keeps *linear* sequence cost without quadratic attention [33]. (2) Versus SSM-only designs (Pan-Mamba, FusionMamba), we explicitly disentangle spectra and space via 2D/1D Haar pyramids before cross-modal fusion [10]. (3) Versus model-driven/unfolding and content-adaptive non-local approaches, S2WMamba performs *subband-wise* dual-branch fusion that improves spectral fidelity at similar model size [5]. Lightweight LGP-Conv is efficient, yet our method attains higher accuracy with comparable parameters.

### 3.2. Datasets and Benchmark

We evaluate our method on datasets from the WorldView-3 (WV3) and GaoFen-2 (GF2) and QuickBird (QB) sensors. These datasets are available at <https://github.com/liangjiandeng/PanCollection>. Following Wald’s protocol [29], we generate training pairs of PAN, LRMS, and ground truth (GT) images at reduced resolution. For instance, the WV3 dataset uses image sizes of

64×64 (PAN), 16×16×8 (LRMS), and 64×64×8 (GT). All datasets and processing steps are sourced from the PanCollection repository[4]. We compared against several state-of-the-art methods, including traditional (MTF-GLP-FS [27], BDS-PC [26], TV [21]) and deep learning-based approaches (PNN [19], PanNet [32], DiCNN [12], FusionNet [3], PanMamba [10], CANNNet [5], U2Net [22], and FusionMamba [23]).

### 3.3. Implementation Details

Our network was implemented in PyTorch and trained on an RTX 4090 24GB GPU. We used the AdamW optimizer [17] with a learning rate of  $4 \times 10^{-4}$ , which decayed by a factor of 0.7 every 100 epochs, for a total of 360 epochs with a batch size of 32. The performance was assessed using standard metrics: SAM [2], ERGAS [28], and Q4/Q8 [8] for reduced-resolution tests, and HQNR [1],  $D_s$ , and  $D_\lambda$  for full-resolution tests.

#### 3.3.1. Reduced-Resolution Assessment

As shown in Tab. 3, our method consistently outperforms all benchmarks, demonstrating the superiority and universality of our network, while FusionMamba or CANNNet outperforms on only one or two datasets. Notably, S2WMamba achieves PSNR improvements of 0.231 dB on GF2, 0.045 dB on QB, and 0.021 dB on WV3 over the second-best methods. The qualitative results in Fig. 6 corroborate these findings; the residual map for our method is the darkest, indicating the highest fidelity to the ground truth and confirming its superior performance.

#### 3.3.2. Full-Resolution Assessment

To evaluate real-world applicability, we conducted experiments on full-resolution WV3 samples. As detailed in Tab. 4, our method achieves the highest HQNR score, demonstrating an optimal balance between spectral and spatial fidelity.

Furthermore, S2WMamba achieves this state-of-the-art performance with high efficiency. Its 0.63M parameters for the WV3 configuration are fewer than those of other top performers like FusionMamba (0.73M) and U2Net (0.66M). While PanMamba (0.48M) is smaller, our method leads substantially across all metrics. This proves that S2WMamba’s superiority stems from its advanced architectural design, not merely from an increased parameter count, establishing an excellent balance between performance and efficiency.

### 3.4. Ablation Study

We conducted comprehensive ablation studies on the WV3 dataset to validate S2WMamba’s architectural components. The results, summarized in Tab. 5, are analyzed by grouping experiments into three core aspects: the dual-branch architecture, the State Space Model (SSM) backbone, and the

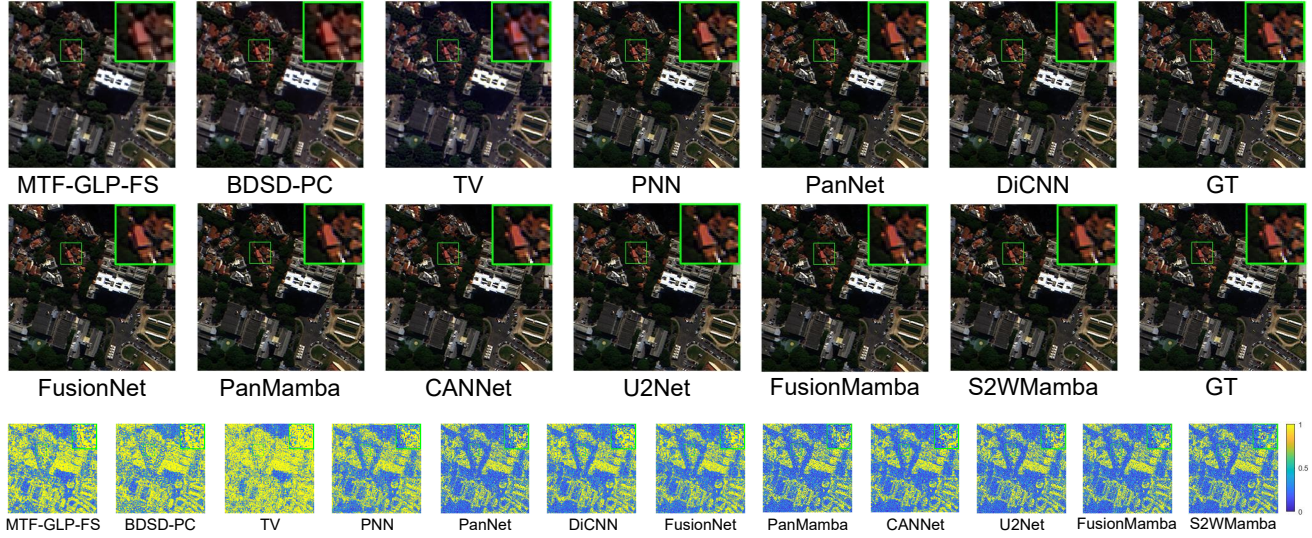


Figure 6. The visual results (Top) and residuals (Bottom) of all compared approaches on the WV3 reduced-resolution dataset.

Methods	WV3				GF2				QB			
	PSNR $\uparrow$	SAM $\downarrow$	ERGAS $\downarrow$	Q8 $\uparrow$	PSNR $\uparrow$	SAM $\downarrow$	ERGAS $\downarrow$	Q4 $\uparrow$	PSNR $\uparrow$	SAM $\downarrow$	ERGAS $\downarrow$	Q4 $\uparrow$
MTF-GLP-FS	32.963	5.316	4.700	0.833	41.565	1.655	1.589	0.897	32.709	7.792	7.373	0.835
BSDS-PC	32.970	5.428	4.697	0.829	41.205	1.681	1.667	0.892	32.550	8.085	7.513	0.831
TV	32.381	5.692	4.855	0.795	41.262	1.911	1.737	0.907	32.136	7.510	7.690	0.821
PNN	37.313	3.677	2.681	0.893	45.096	1.048	1.057	0.960	36.942	5.181	4.468	0.918
PanNet	37.346	3.613	2.664	0.891	46.268	0.997	0.919	0.967	34.678	5.767	5.859	0.885
DiCNN	37.390	3.592	2.672	0.900	44.931	1.053	1.081	0.959	35.781	5.367	5.133	0.904
FusionNet	38.047	3.324	2.465	0.904	45.663	0.974	0.988	0.964	37.540	4.904	4.156	0.925
PanMamba	39.012	2.913	2.184	0.920	48.931	0.743	0.684	0.982	37.356	4.625	4.277	0.929
CANNet	39.003	2.941	2.174	0.920	49.520	0.707	0.630	<u>0.983</u>	<u>38.488</u>	<u>4.496</u>	<u>3.698</u>	<u>0.937</u>
U2Net	39.117	2.888	2.150	0.920	49.404	0.714	0.632	0.982	38.065	4.642	3.987	0.931
FusionMamba	<u>39.374</u>	<u>2.844</u>	<u>2.092</u>	<u>0.922</u>	<u>49.678</u>	<u>0.705</u>	<u>0.615</u>	<b>0.984</b>	37.986	4.610	4.054	0.930
<b>S2WMamba</b>	<b>39.391</b>	<b>2.825</b>	<b>2.087</b>	<b>0.923</b>	<b>49.909</b>	<b>0.676</b>	<b>0.599</b>	<b>0.984</b>	<b>38.533</b>	<b>4.445</b>	<b>3.679</b>	<b>0.938</b>

Table 3. Comparisons on WV3, GF2 and QB datasets with 20 reduced-resolution samples, respectively. Best: **bold**, and second-best: underline.

fusion strategy. This grouped analysis systematically justifies the design of our model.

**Effectiveness of the Dual-Branch Architecture.** These experiments validate the fundamental design of our parallel, dual-branch framework. Evaluating each branch in isolation, the **SpeO** (Spectral Branch Only) variant suffered from a loss of fine textures, while the **SpaO** (Spatial Branch Only) variant exhibited significant spectral distortion. These results confirm that the branches are codependent and indispensable for balancing spatial detail and spectral fidelity. Finally, the **SeqB1** (Sequential Branches) and **SeqB2** variant, using sequential pipelines, underperformed compared to our parallel design, proving that parallel pro-

cessing with final fusion module offers a more flexible and powerful integration strategy.

**Contribution of the Mamba Backbone.** The contribution of the Mamba backbone was verified in the **CRM** (Convolution Replace Mamba) experiment, where replacing FMamba modules with standard convolutional blocks caused a significant performance drop. This result highlights the limitations of CNNs’ local receptive fields and confirms that Mamba’s capacity for modeling long-range dependencies is crucial for capturing the global context and complex interactions between frequency sub-bands in our framework.

Metric	M-G-FS	B-PC	TV	PNN	PanNet	DiCNN	FusionNet	U2Net	PanM	CANNet	FusionM	Ours
$D_\lambda \downarrow$	0.020	0.063	0.023	0.021	<b>0.017</b>	0.036	0.024	0.020	<u>0.018</u>	0.020	0.019	0.024
$D_s \downarrow$	0.063	0.073	0.039	0.043	0.047	0.046	0.036	0.028	0.053	0.030	<u>0.027</u>	<b>0.021</b>
HQNR $\uparrow$	0.919	0.870	0.938	0.937	0.937	0.920	0.941	0.952	0.930	0.951	<u>0.955</u>	<b>0.956</b>

Table 4. Quantitative comparisons on the WV3 full-resolution dataset. (Some names of the algorithms are abbreviated due to table length issue.)

Ablation	PSNR $\uparrow$	SAM $\downarrow$	ERGAS $\downarrow$	Q8 $\uparrow$
SpeO	38.769	3.100	2.252	0.916
SpaO	38.734	3.010	2.259	0.916
SeqB1	39.193	2.876	2.136	0.921
SeqB2	39.105	2.969	2.163	0.918
CRM	38.870	2.986	2.244	0.919
HP	38.681	3.118	2.230	0.916
AWS	38.702	3.108	2.275	0.917
no Gm	39.233	2.899	2.127	0.921
no Gc	39.186	2.943	2.154	0.920
no Ga	39.179	2.969	2.170	0.920
<b>Orig</b>	<b>39.391</b>	<b>2.825</b>	<b>2.087</b>	<b>0.923</b>

Table 5. Ablation experiment about key components and strategy on WV3 reduced-resolution dataset.

**Efficacy of the Fusion Strategy.** This set of experiments assesses our dual Multi-Scale Dynamic Gate (MSDG) against alternative fusion mechanisms. The **HP** (Hadamard Product) variant, replacing the dual MSDG with a simple Hadamard product, led to a notable performance decline, proving that simple linear interaction is insufficient. The **AWS** (Attention-Weighted Sum) variant also yielded inferior results, suggesting that adaptive linear combinations cannot capture the required complex, non-linear relationships. Then we did a few ablation studies inside the gate named **no Gm**, **no Gc**, **no Ga**, and these studies proves the effectiveness of all the three gates. Collectively, these results validate that our dual MSDG strikes an effective balance, providing powerful, adaptive, non-linear fusion without unnecessary complexity.

## 4. Conclusion

In this paper, we propose S2WMamba, a novel dual-branch architecture that tackles multi-modal feature fusion by performing decomposition and reconstruction in the wavelet domain. By uniquely employing a 2D DWT to inject spatial details and a novel 1D DWT to preserve spectral consistency, S2WMamba achieves more effective and precise fusion. Our framework’s efficacy is further enhanced by FusionMamba modules for efficient long-range dependency modeling and a comprehensive Multi-Scale Dynamic Gate for adaptive fusion. We believe this paradigm of wavelet-based feature disentanglement coupled with efficient long-range modeling offers a promising blueprint

for other challenging multi-modal fusion tasks. Comprehensive ablation studies validate our design, and extensive experiments on multiple satellite datasets demonstrate that our model outperforms state-of-the-art methods.

## References

- [1] Andrea Arienzo, Giuseppe Scarpa, Gemine Vivone, and Luciano Alparone. A full-resolution quality index for pansharpened images. *IEEE Transactions on Geoscience and Remote Sensing*, 60:1–13, 2022. 6
- [2] Joseph W Boardman. Automated spectral unmixing of aviris data using convex geometry concepts. *Summaries of the fourth annual JPL airborne geoscience workshop*, 1:11–14, 1993. 6
- [3] Liang-Jian Deng, Gemine Vivone, Chen Jin, Manuele E Paoletti, Xiang Zhuo, and Jocelyn Chanussot. Fusionnet: A two-stage fusion network for pansharpening. *IEEE Transactions on Geoscience and Remote Sensing*, 60:1–16, 2021. 6
- [4] Liang-Jian Deng, Gemine Vivone, Manuele E Paoletti, Giuseppe Scarpa, Jun He, Le Zhang, and Jocelyn Chanussot. Machine learning in pansharpening: A benchmark, from shallow to deep networks. *IEEE Geoscience and Remote Sensing Magazine*, 10(4):349–384, 2022. 6
- [5] Yule Duan, Jie Huang, Rui Huang, and Liang-Jian Deng. Cannet: A channel attention-based network for pansharpening. *arXiv preprint arXiv:2403.04803*, 2024. 6
- [6] Yule Duan, Xiao Wu, Haoyu Deng, and Liang-Jian Deng. Content-adaptive non-local convolution for remote sensing pansharpening. In *Proceedings of the IEEE/CVF Conference on Computer Vision and Pattern Recognition*, pages 27738–27747, 2024. 2
- [7] Shin Fujieda, Kohei Takayama, and Toshiya Hachisuka. Wavelet convolutional neural networks. *arXiv preprint arXiv:1805.08620*, 2018. 2
- [8] Andrea Garzelli and Filippo Nencini. A comparative study of pansharpening algorithms based on the f-norm. *IEEE Geoscience and Remote Sensing Letters*, 6(4):822–826, 2009. 6
- [9] Albert Gu and Tri Dao. Mamba: Linear-time sequence modeling with selective state spaces. *arXiv preprint arXiv:2312.00752*, 2023. 2
- [10] Jun He, Siran Peng, Haoyu Deng, and Liang-Jian Deng. Panmamba: A new state-of-the-art for pansharpening. *arXiv preprint arXiv:2403.11637*, 2024. 1, 6
- [11] Kaiming He, Xiangyu Zhang, Shaoqing Ren, and Jian Sun. Deep residual learning for image recognition. In *Proceedings of the IEEE conference on computer vision and pattern recognition*, pages 770–778, 2016. 6

- [12] Lei He, Yumo Rao, Jiayi Li, Jonathan Cheung-Wai Chan, Antonio J Plaza, Qing Zhu, and Shutao Li. Dcn: A detail-injection-based convolutional neural network for pansharpening. In *IGARSS 2019-2019 IEEE International Geoscience and Remote Sensing Symposium*, pages 1701–1704. IEEE, 2019. 6
- [13] Jie Huang, Rui Huang, Jinghao Xu, Siran Peng, Yule Duan, and Liang-Jian Deng. Wavelet-assisted multi-frequency attention network for pansharpening. In *Proceedings of the AAAI Conference on Artificial Intelligence*, pages 3662–3670, 2025. 2
- [14] Phillip Isola, Jun-Yan Zhu, Tinghui Zhou, and Alexei A Efros. Image-to-image translation with conditional adversarial networks. In *Proceedings of the IEEE conference on computer vision and pattern recognition*, pages 1125–1134, 2017. 6
- [15] Ting Li, Jiayi Ma, and Hong Zhang. Msdcnn: A novel multi-scale dilated convolutional neural network for pansharpening. *International Journal of Remote Sensing*, 39(18):6080–6097, 2018. 1
- [16] Yue Liu, Yunjie Tian, Yuzhong Zhao, Hongtian Yu, Lingxi Xie, Yaowei Wang, Qixiang Ye, Jianbin Jiao, and Yunfan Liu. Vmamba: Visual state space model. *Advances in neural information processing systems*, 37:103031–103063, 2024. 1
- [17] Ilya Loshchilov and Frank Hutter. Decoupled weight decay regularization. *arXiv preprint arXiv:1711.05101*, 2017. 6
- [18] Stephane G Mallat. A theory for multiresolution signal decomposition: the wavelet representation. *IEEE transactions on pattern analysis and machine intelligence*, 11(7):674–693, 1989. 2
- [19] Giuseppe Masi, Davide Cozzolino, Luisa Verdoliva, and Giuseppe Scarpa. Pansharpening by convolutional neural networks. In *2016 23rd International conference on pattern recognition (ICPR)*, pages 1650–1655. IEEE, 2016. 1, 6
- [20] Nikolaos Ntantis, Jasper S Wijnands, Jan Fokke Meirink, and Domenica Dibenedetto. A cross-band transformer on wavelets for pansharpening of satellite imagery. *European Journal of Remote Sensing*, 58(1):2495314, 2025. 2
- [21] Finnbogi Palsson, Johannes R Sveinsson, and Magnus O Ulfarsson. A variational approach for pansharpening. *IEEE Transactions on Geoscience and Remote Sensing*, 51(10):5287–5296, 2013. 6
- [22] Siran Peng, Haoyu Deng, and Liang-Jian Deng. U2net: A u-shaped network with an enhanced cross-attention module for pansharpening. *arXiv preprint arXiv:2310.02157*, 2023. 6
- [23] Siran Peng, Xiangyu Zhu, Haoyu Deng, Liang-Jian Deng, and Zhen Lei. Fusionmamba: Efficient remote sensing image fusion with state space model. *IEEE Transactions on Geoscience and Remote Sensing*, 62:1–16, 2024. 1, 2, 6
- [24] Jing Tian, Wei Ma, Le Zhang, Ce Zhao, and Hongyan Zhang. A variational framework for pansharpening. *IEEE Transactions on Geoscience and Remote Sensing*, 60:1–15, 2022. 1
- [25] Ashish Vaswani, Noam Shazeer, Niki Parmar, Jakob Uszkoreit, Llion Jones, Aidan N Gomez, Łukasz Kaiser, and Illia Polosukhin. Attention is all you need. In *Advances in neural information processing systems*, pages 5998–6008, 2017. 1
- [26] Gemine Vivone. Component-substitution-based pansharpening from a variational perspective. *IEEE Transactions on Geoscience and Remote Sensing*, 57(9):6728–6743, 2019. 1, 6
- [27] Gemine Vivone, Rocco Restaino, and Jocelyn Chanussot. A multiresolution analysis-based pansharpening method with a hybrid injection model. *IEEE Transactions on Geoscience and Remote Sensing*, 56(10):5923–5936, 2018. 1, 6
- [28] Lucien Wald. Data fusion: a conceptual approach for an efficient assessment of the quality of the resulting images. *Data fusion for situation monitoring, incident detection, alert and response management*, 2:19–24, 2002. 6
- [29] Lucien Wald, Thierry Ranchin, and Marc Mangolini. Fusion of satellite images of different spatial resolutions: Assessing the quality of resulting images. *Photogrammetric engineering and remote sensing*, 63(6):691–699, 1997. 6
- [30] Xueyang Wang, Zhixin Zheng, Jiandong Shao, Yule Duan, and Liang-Jian Deng. Adaptive rectangular convolution for remote sensing pansharpening. In *Proceedings of the Computer Vision and Pattern Recognition Conference*, pages 17872–17881, 2025. 2
- [31] Fei Xie, Jiahao Nie, Yujin Tang, Wenkang Zhang, and Hongshen Zhao. Mamba-adaptor: State space model adaptor for visual recognition. In *Proceedings of the Computer Vision and Pattern Recognition Conference*, pages 20124–20134, 2025. 1
- [32] J Yang, X Fu, Y Hu, Y Huang, X Ding, and J Paisley. Pan-net: A deep network architecture for pan-sharpening. *Proceedings of the IEEE international conference on computer vision*, pages 5449–5457, 2017. 6
- [33] Hui Zhou, Zipeng Liu, and Huiren Wang. Panformer: A transformer-based pan-sharpening method for remote sensing images. In *Proceedings of the 30th ACM International Conference on Multimedia*, pages 4773–4782, 2022. 1, 6
- [34] Man Zhou, Jie Huang, Yanchi Fang, Xueyang Fu, and Aiping Liu. Pan-sharpening with customized transformer and invertible neural network. In *Proceedings of the AAAI conference on artificial intelligence*, pages 3553–3561, 2022. 2

# S2WMamba: A Spectral-Spatial Wavelet Mamba for Pansharpening

## Supplementary Material

### Abstract

This supplementary material provides additional details on S2WMamba. We begin with a detailed explanation of the 1D/2D Discrete Wavelet Transforms (DWT), the FMamba module and the multi-scale strategy. We then offer an in-depth analysis of the ablation studies, justifying each architectural component. A comparison of model parameters highlights our method's efficiency. Finally, additional qualitative results, including residual and HQNR maps for multiple datasets, are provided to further validate the model's superior performance and robustness.

## 5. Method Supplementary

### 5.1. Detailed Explanation of 2D Discrete Wavelet Transform (DWT2D)

To illustrate the process of the two-dimensional Discrete Wavelet Transform (DWT2D), we consider a simple example for ease of understanding. Suppose we have a single-channel image consisting of only four pixels, which can be represented as a  $2 \times 2$  matrix:

$$I = \begin{bmatrix} a_{11} & a_{12} \\ a_{21} & a_{22} \end{bmatrix} \quad (11)$$

Applying the DWT2D to this image yields four sub-band components: the low-frequency component (LL) and three high-frequency components corresponding to the horizontal (LH), vertical (HL), and diagonal (HH) directions. Each of these sub-bands has a spatial resolution reduced by half (i.e.,  $1 \times 1$  in this case). The computation of each component is given as follows:

$$LL = \frac{a_{11} + a_{12} + a_{21} + a_{22}}{4} \quad (12)$$

$$LH = \frac{a_{11} + a_{12} - a_{21} - a_{22}}{4} \quad (13)$$

$$HL = \frac{a_{11} - a_{12} + a_{21} - a_{22}}{4} \quad (14)$$

$$HH = \frac{a_{11} - a_{12} - a_{21} + a_{22}}{4} \quad (15)$$

For a larger image, the input is first divided into multiple non-overlapping  $2 \times 2$  blocks. The above transformation is then applied independently to each block. The resulting  $LL$ ,  $LH$ ,  $HL$ , and  $HH$  components from all blocks are then respectively spatially arranged according to their original positions to form four complete sub-band images:  $LL$ ,  $LH$ ,

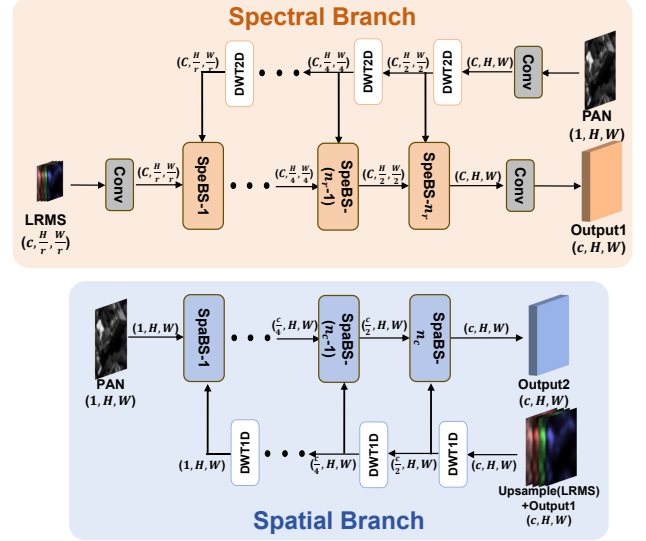


Figure 7. The explanation of the multi-scale processing in Spectral Branch and Spatial Branch adopted in our method. The dimensions above the arrows represent the data dimensions entering the module to which the arrow points. In this paper,  $C = 32$ .

HL and HH, corresponding to the DWT2D decomposition of the original image.

The original image can be reconstructed by applying the inverse transform (IDWT2D), which linearly combines the  $LL$ ,  $LH$ ,  $HL$ , and  $HH$  components. In practice, these operations can be efficiently implemented using fixed-value convolution and deconvolution kernels.

### 5.2. Detailed Explanation of 1D Discrete Wavelet Transform (DWT1D)

To illustrate the process of the one-dimensional Discrete Wavelet Transform (DWT1D), we follow a similar explanatory approach. This transform operates along the channel axis to disentangle spectral information. For a simple example, let's consider the spectral values at a single pixel location from an image with two channels. These values can be represented as a 1D vector:

$$I_{\text{pixel}} = [c_1, c_2] \quad (16)$$

Applying the 1D Haar DWT to this vector yields two components: a low-frequency component (L), representing the average spectral value, and a high-frequency component (H), representing the spectral variation. The number of channels is halved for each component, and the compu-

tation is as follows:

$$L = \frac{c_1 + c_2}{2} \quad (17)$$

$$H = \frac{c_1 - c_2}{2} \quad (18)$$

For a full image tensor with an even number of channels  $C$  (e.g., shape  $B \times C \times H \times W$ ), the 1D DWT is applied independently to the channel vector at each spatial position. The operation processes adjacent pairs of channels across the entire channel dimension. The resulting low-frequency components from all pairs are grouped to form the L sub-band, and the high-frequency components form the H sub-band. Both sub-bands have a shape of  $B \times (C/2) \times H \times W$ . These are then concatenated along the channel dimension to produce the final output.

The original spectral information can be perfectly reconstructed by applying the inverse transform (IDWT1D), which linearly combines the L and H components. In practice, these operations are efficiently implemented using fixed-filter 1D convolutions and transposed convolutions along the channel axis.

### 5.3. Multi-Scale Strategy Details

The multi-scale characteristic of the wavelet pyramid allows for more effective utilization of features across different scales. The multi-scale fusion process we adopt in Spectral Branch and Spatial Branch is illustrated in Fig. 7.

In Spectral Branch, using multiple DWT2D operations, we obtain spatial detail from PAN image with gradually decreasing resolution until they match the resolution of the LRMS. Fusion begins at the smallest resolution and progressively transitions to the final resolution.

In Spatial Branch, using multiple DWT1D operations, we obtain spectral detail with gradually decreasing channel until they match the channel of the PAN. Fusion begins at the smallest channel and progressively transitions to the final channel.

### 5.4. Detailed Architecture of the Adapted FMamba Block

In this section, we provide a detailed architectural breakdown of our proposed FMamba block. Our design enhances the original FusionMamba (Peng et al. 2024) by replacing its static averaging fusion with a dynamic, learnable mechanism composed of a MixGate module and an adaptive skip connection. This allows the model to intelligently arbitrate information flow between the two modalities (e.g., PAN and MS) in a content-aware manner.

First, we incorporate modality-specific skip connections to preserve initial feature characteristics:

$$X'_{\text{pan}} = X_{\text{pan}} + X_{\text{pan, skip}} \quad (19)$$

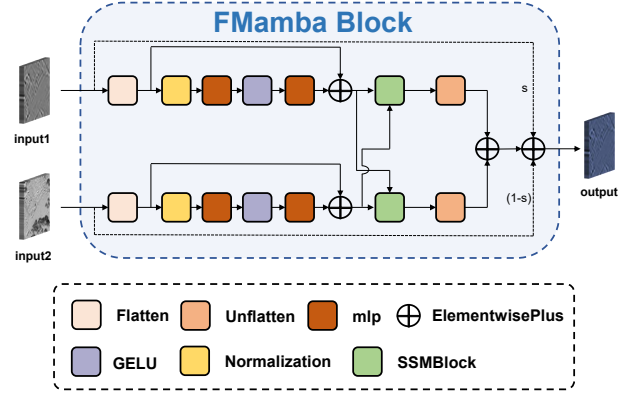


Figure 8. The figure illustrates the architecture of our proposed FusionMamba module. The FusionMamba module uses a dual-stream architecture to fuse panchromatic (PAN) and multispectral (MS) images. Each stream extracts features using SingleMamba blocks. Two CrossMamba blocks then perform interactive fusion, and their outputs are summed with a weighted skip connection for the final result.

$$X'_{\text{ms}} = X_{\text{ms}} + X_{\text{ms, skip}} \quad (20)$$

where  $X_{\text{pan, skip}}$  and  $X_{\text{ms, skip}}$  denote the skip connection features for PAN and MS modalities, respectively.

As in the original work, we employ two parallel CrossMamba modules to achieve bidirectional fusion. Using the updated feature streams ( $X'_{\text{pan}}$  and  $X'_{\text{ms}}$ ), we generate a spatial-primary fusion output ( $F_{\text{sps}}$ ) and a spectral-primary fusion output ( $F_{\text{spe}}$ ):

$$F_{\text{sps}} = \text{CrossMamba}(X'_{\text{pan}}, X'_{\text{ms}}) \quad (21)$$

$$F_{\text{spe}} = \text{CrossMamba}(X'_{\text{ms}}, X'_{\text{pan}}) \quad (22)$$

For the final fusion step, we introduce a learnable skip connection that dynamically combines the original feature streams using a sigmoid-gated weight parameter  $\alpha$ :

$$S = \sigma(\alpha) \cdot X'_{\text{pan}} + (1 - \sigma(\alpha)) \cdot X'_{\text{ms}} \quad (23)$$

The final fused output is obtained by summing the bidirectional fusion results with this adaptive skip connection:

$$F_{\text{final}} = F_{\text{sps}} + F_{\text{spe}} + S \quad (24)$$

Finally, we reshape the feature maps back to their original spatial dimensions for subsequent processing:

$$X_{\text{pan, out}} = \text{rearrange}(X'_{\text{pan}}, 'b(hw)c \rightarrow bchw') \quad (25)$$

$$X_{\text{ms, out}} = \text{rearrange}(X'_{\text{ms}}, 'b(hw)c \rightarrow bchw') \quad (26)$$

$$F_{\text{out}} = \text{rearrange}(F_{\text{final}}, 'b(hw)c \rightarrow bchw') \quad (27)$$

where  $\text{rearrange}(\cdot)$  denotes the operation that reshapes sequence-form features back to spatial-form feature maps with height  $h$  and width  $w$ .

## 6. Experimental Supplementary

### 6.1. Comparison of Parameter Numbers

To provide a clear perspective on model efficiency, we compare the parameter counts of our proposed S2WMamba with other leading deep learning-based pansharpening methods. As shown in Table 6, S2WMamba achieves state-of-the-art performance without an excessive number of parameters. It is more efficient than other high-performing models like CANNet and FusionMamba. This highlights that the performance gains of our model stem from its advanced architectural design—specifically, the principled feature disentanglement in the wavelet domain—rather than sheer model size. This demonstrates an excellent balance between performance and computational efficiency.

Methods	Params(M)
PNN	0.10
PanNet	0.08
DiCNN	0.04
FusionNet	0.08
U2Net	0.66
PanMamba	0.48
CANNet	0.78
FusionMamba	0.73
<b>S2WMamba (Ours)</b>	<b>0.60</b>

Table 6. Comparison of parameters (in millions) for different deep learning-based methods, configured for the WV3 dataset.

### 6.2. Ablation Study Details

This section provides a more detailed explanation of the ablation experiments presented in the main paper to validate the key components of our S2WMamba architecture. Each experiment systematically modifies a part of the model to isolate its contribution.

**Effectiveness of the Dual-Branch Architecture.** These experiments assess the foundational parallel, dual-branch design.

- **SpeO (Spectral Branch Only):** In this variant, the Spatial Branch and the Multi-Scale Dynamic Gate (MSDG) were removed. The final output of the Spectral Branch was directly passed through a concluding convolutional layer to produce the residual image. The resulting performance drop confirms the necessity of the Spatial Branch for injecting spectrally-guided structural refinements.
- **SpaO (Spatial Branch Only):** Here, the Spectral Branch was removed. The input to the 1D Wavelet Pyramid Construction (1DWPC) in the Spatial Branch was sourced directly from the upsampled LRMS image, without the additive enhancement from the Spectral Branch’s output.

The significant color distortion observed underscores the critical role of the Spectral Branch in preserving spectral fidelity.

- **RAC (Remove Additional Connection):** We removed the additive link from the Spectral Branch to the Spatial Branch. Specifically, the input to the 1DWPC became  $L_0 = \text{Upsample}(\text{LRMS})$  instead of  $L_0 = \text{Upsample}(\text{LRMS}) + \text{Output}_1$ . The degraded performance highlights that this connection is crucial for providing the Spatial Branch with a spatially-enhanced feature map, guiding a more effective spectral refinement.
- **SwapB (Swapped Branches):** This experiment inverted the information flow. The Spatial Branch first processed the PAN and LRMS images, and its output was then used to guide the Spectral Branch. The inferior results validate our original design, where enriching the MS features with spatial details first provides a better foundation for subsequent fusion.
- **SeqB (Sequential Branches):** We replaced the parallel architecture with a sequential pipeline where the output of the first branch (e.g., Spectral) becomes the primary input for the second (e.g., Spatial). The underperformance of this variant proves that our parallel design, combined with the MSDG, allows for a more flexible and powerful integration of the disentangled features.

**Contribution of the Mamba Backbone.** This experiment validates the choice of Mamba as the core for long-range dependency modeling.

- **CRM (Convolution Replace Mamba):** All FMamba modules within both the Spectral and Spatial Branches were replaced with standard residual convolutional blocks (each containing two 3x3 convolutions with a GELU activation). The significant performance drop demonstrates that the local receptive fields of CNNs are insufficient for capturing the complex, long-range interactions between frequency sub-bands, confirming that Mamba’s global context modeling is essential to our framework’s success.

**Efficacy of the Fusion Strategy.** This group of experiments justifies our choice of the Multi-Scale Dynamic Gate (MSDG) over simpler fusion mechanisms.

- **HP (Hadamard Product):** The MSDG was replaced with a simple element-wise multiplication between the outputs of the two branches ( $\text{Output}_1 \odot \text{Output}_2$ ). The performance decline shows that a simple linear interaction is inadequate for fusing the complex features.
- **AWS (Attention-Weighted Sum):** We replaced the MSDG with an adaptive weighted sum, where the weights were generated by a simple channel-attention mechanism applied to the concatenated features. The inferior result suggests that a linear combination, even if adaptive, cannot model the non-linear, spatially varying relationships

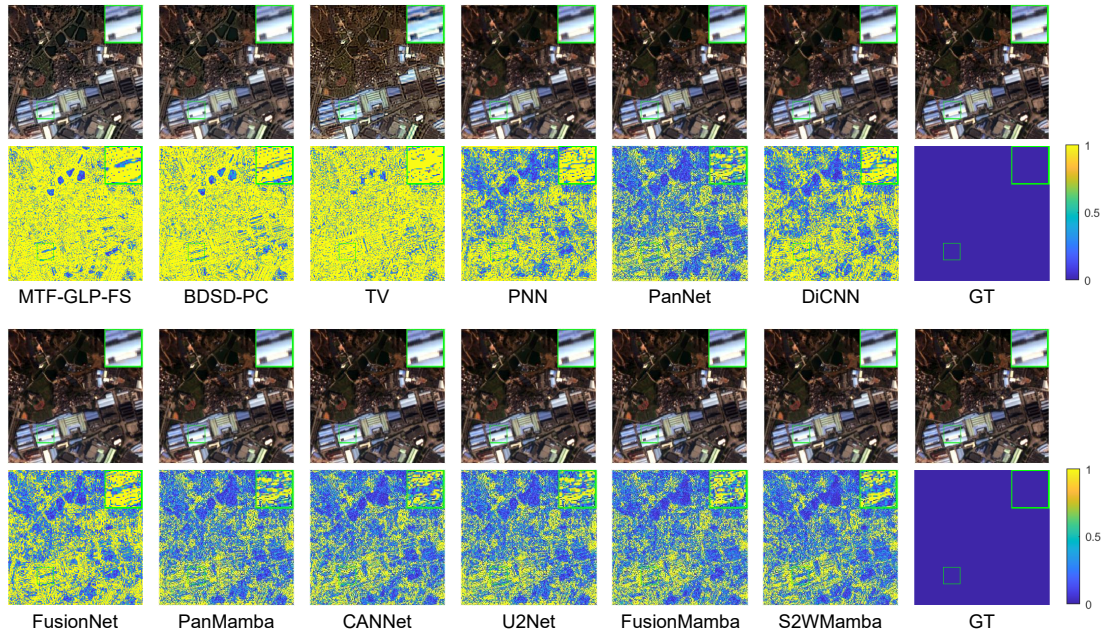


Figure 9. Qualitative comparison on the GF2 reduced-resolution dataset. The top row displays the pansharpened images generated by different methods, while the bottom row shows the corresponding residual maps (difference from Ground Truth). A darker residual map indicates a smaller error and higher fidelity. Our S2WMamba produces the result with the least residual error, demonstrating superior reconstruction accuracy.

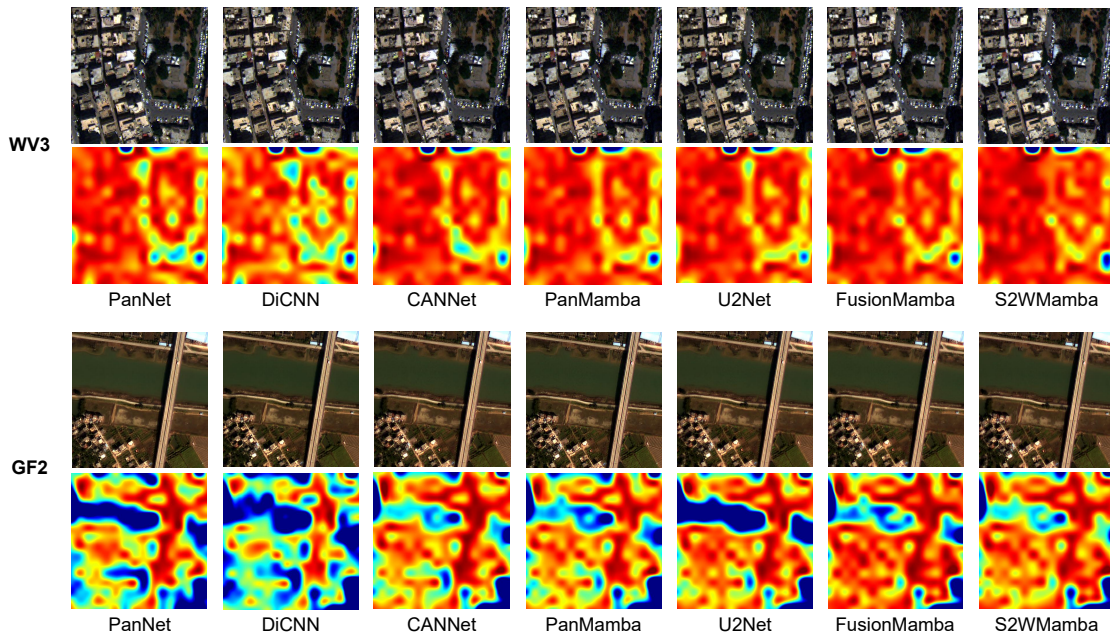


Figure 10. Visualization of the HQNR metric on the full-resolution WV3 (top) and GF2 (bottom) datasets. The heatmaps represent the spatial distribution of the HQNR scores for various methods. Redder areas indicate higher HQNR values (better quality), while bluer areas indicate lower values. S2WMamba consistently shows larger and more intensely red regions across both datasets, visually confirming its superior performance and robust balance between spatial and spectral quality in real-world scenarios.

required for optimal fusion.

- **DPG (Dual Parallel Gates):** In this variant, we used an overly complex fusion module with conflicting optimization paths. This created "model confusion," leading to underperformance. This result, alongside the others, validates that our MSDG strikes an effective balance, offering powerful, adaptive, and non-linear fusion without being unnecessarily complex.

### 6.3. Additional Qualitative Results

To further demonstrate the effectiveness of our proposed S2WMamba, we provide additional qualitative results in this section. Figure 9 presents a visual comparison of our method against several state-of-the-art approaches on the GF2 dataset. The residual maps clearly show that S2WMamba achieves the lowest error when compared to the ground truth, indicating a more accurate fusion of spatial details and spectral information.

Furthermore, Figure 10 offers a compelling visualization of the full-resolution assessment on both WV3 and GF2 datasets using HQNR heatmaps. This metric evaluates the overall quality by balancing spectral and spatial fidelity. The predominantly red areas in the S2WMamba results signify consistently high quality across the entire image, outperforming other methods which exhibit more blue and green areas, indicative of lower quality and distortion. These visual proofs corroborate the quantitative results in the main paper and highlight the robustness and superiority of our method.